

NeB-SLAM: Neural Blocks-based Salable RGB-D SLAM for Unknown Scenes

Lizhi Bai, Chunqi Tian*, Jun Yang, Siyu Zhang, Weijian Liang

Abstract—Neural implicit representations have recently demonstrated considerable potential in the field of visual simultaneous localization and mapping (SLAM). This is due to their inherent advantages, including low storage overhead and representation continuity. However, these methods necessitate the size of the scene as input, which is impractical for unknown scenes. Consequently, we propose NeB-SLAM, a neural block-based scalable RGB-D SLAM for unknown scenes. Specifically, we first propose a divide-and-conquer mapping strategy that represents the entire unknown scene as a set of sub-maps. These sub-maps are a set of neural blocks of fixed size. Then, we introduce an adaptive map growth strategy to achieve adaptive allocation of neural blocks during camera tracking and gradually cover the whole unknown scene. Finally, extensive evaluations on various datasets demonstrate that our method is competitive in both mapping and tracking when targeting unknown environments.

Index Terms—Neural RGB-D SLAM, dense mapping.

I. INTRODUCTION

DENSE visual simultaneous localization and mapping (SLAM) is an essential technology in 3D computer vision for a number of applications in autonomous driving, robotics, mixed reality, and other fields. Considering the complexity of real world application scenarios, dense vision SLAM is expected to reconstruct high-quality 3D dense scenes while maintaining real-time performance, which can be scaled to unknown environments while sensing invisible regions.

As a branch of visual SLAM, RGB-D visual SLAM technology has been fully developed over the past decade since the pioneering work of KinectFusion [1], [2]. Traditional RGB-D SLAM methods [1]–[5] have the advantage of maintaining an efficient computational cost while being able to estimate the camera pose with high accuracy and robustness in a wide range of large-scale unknown scenarios. However, these approaches are incapable of making reasonable geometric inference for invisible regions, so that the reconstructed 3D maps have some empty regions, and in addition, dense maps for large scenes require high storage costs.

Recently, neural implicit 3D scene representation or reconstruction has received a lot of attentions [6]–[9], especially the advent of neural radiance fields (NeRF) [10] has brought 3D scene representation to a new level of excitement. NeRF represents a continuous scene as an end-to-end learnable neural network. Specifically, NeRF characterizes the 3D space using a 5D vector-value (3D position and 2D view direction)

function and fits it through a compact multilayer perceptron (MLP) to map the corresponding volume densities and colors, optimizing the 3D scene representation by minimizing the rendering error of the network. Neural networks come with an inference capability that can, to some extent, fill in the unobserved areas in 3D space, while having an inherent advantage in terms of storage requirements.

NeRF’s strong 3D spatial representation capability is applied to the field of dense vision SLAM for the first time by iMAP [11]. For small-sized rooms, this method demonstrates strong tracking and mapping performance. However, when scaling up to larger scenes, using a single MLP to represent the entire scene is clearly limited. The limited number of individual MLP parameters can lead to catastrophic forgetting of the observed region. This results in a significant degradation in the approach’s tracking and mapping performance. In light of this, some methods [12]–[16] have attempted to use multi-resolution grid features to obtain a more detailed representation of the scene. This allows for an extension of their approach to larger scenes. All of these methods have a restriction that the size of the scene must be known in order to normalize a bounding box. Therefore, these methods are only applicable in known scenes, not in unknown ones.

To realize neural dense visual SLAM that is scalable to unknown scenes, we propose NeB-SLAM, an end-to-end neural RGB-D visual SLAM system. Our approach revolves around a divide-and-conquer mapping strategy and an adaptive growth strategy for mapping as illustrated in Fig. 1. To analyze an unfamiliar scene, we begin by initializing a neural block (NeB), which is a cube with a fixed size, based on the current camera pose. Our method then adaptively allocates new NeBs as RGB-D image sequences are input, eventually partitioning the entire unknown environment into multiple submaps, also known as NeBs. In our method, each NeB represents the local scene as a multi-resolution hash grid [17], which allows for high convergence speed and the representation of high-frequency local features. Inspired by Co-SLAM [14], each NeB also encodes the coordinates using One-blob [18] to encourage surface coherence. We conducted a comprehensive assessment of numerous indoor RGB-D sequences and showcased the scalability and predictive capabilities of our approach in unfamiliar settings. In summary, our contributions are as follows:

- We propose NeB-SLAM, an end-to-end dense RGB-D SLAM system for unknown scenarios that is real-time, scalable, and predictive.
- For unknown scenarios, we propose a divide-and-conquer mapping strategy and an adaptive map growth strategy to

Lizhi Bai, Chunqi Tian, Jun Yang, Siyu Zhang and Weijian Liang are with Department of Computer Science and Technology, Tongji University, Shanghai, 201804, China (e-mail: {bailizhi, junyang, tianchunqi, 2010149, liangweijian}@tongji.edu.cn).

* Corresponding author

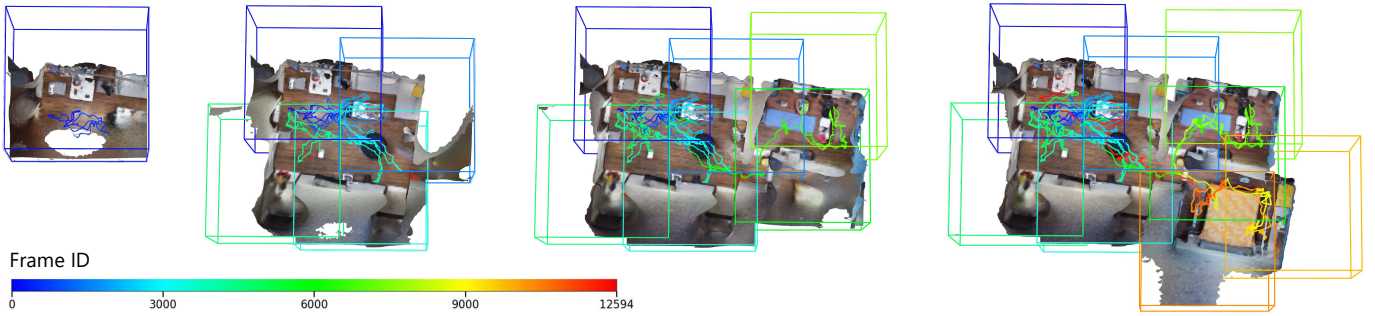


Fig. 1: The divide-and-conquer mapping process for unknown scenes. NeBs are adaptively allocated with camera tracking to gradually cover the entire unknown scene.

achieve full coverage of the unknown environment by the submap during the tracking process.

- Extensive evaluations on various datasets demonstrate that our method is competitive in both mapping and tracking when targeting unknown environments.

II. RELATED WORK

A. Dense Visual SLAM

Thanks to the pioneering work of Klein et al. [19], most current visual SLAM systems are organized into two parts: tracking and mapping. DTAM [20] is an early dense SLAM system that tracks the camera using the photometric consistency of each pixel. It employs multi-view stereo constraints to update the dense scene model and represent it as a cost-volume. KinectFusion [1] takes advantage of RGB-D cameras to enable real-time camera pose estimation and scene geometry updating with iterative closest point (ICP) and TSDF-Fusion [21]. Many subsequent studies have suggested various efficient data structures to enable the scalability of SLAM systems, such as VoxelHash [22]–[24] and Octrees [25], [26].

With the development of deep learning, some works have integrated it into SLAM systems to enhance the robustness and accuracy of conventional methods. DeepTAM [27] is similar to DTAM [20], but it uses convolutional neural networks (CNN) to estimate camera pose increments and depth maps. Comparable approaches are Demon [28] and DeepV2D [29]. CodeSLAM [30] employs a variational auto-encoders [31] to achieve the latent compact representation of scene geometry, reducing the complexity of the problem. There are methods, such as SceneCode [32] and NodeSLAM [33], that optimize the potential features by decoding them into depth maps. BA-Net [34] and DeepFactors [35] simplify the optimization problem by using networks to generate a set of basis depth maps and representing the resulting depth maps as a linear combination of these basis depth maps. Droid-SLAM [36] greatly improves the generalizability of a pre-trained model across scenarios through the use of dense optical flow estimation [37] and dense bundle adjustment, allowing for competitive results in a variety of challenging datasets. Tandem [38] realizes a real-time monocular dense SLAM system by performing frame-to-model photometric tracking to decouple the pose/depth problem using multi-view stereo network and DSO [39].

In contrast to these approaches, ours is an end-to-end method that represents the geometric information of the scene as a set of neural blocks with efficient memory usage and reasonable hole-filling.

B. Neural Implicit Representations

Recently neural implicit representations have gained significant attention, which initially encode the geometric and appearance information of a 3D scene in the parameters of a neural network, and are characterized by high expressiveness and compactness. Among these works, NeRF [10] is a valuable geometric representation for capturing view-dependent accurate photometric synthesis while maintaining multi-view consistency. It has inspired numerous papers that aim to improve 3D reconstruction and reduce training time. NeRF-W [40] proposes a method for synthesizing new views of complex scenes using images captured under natural conditions as datasets. This is achieved by introducing appearance embedding and static-dynamic scene separation. Block-NeRF [41] chunks the environment and represents large-scale scenes with multiple NeRFs. By modeling these NeRFs independently, it improves its ability to represent large scenes and its training speed. To improve training efficiency, NGLOD [42] uses a hierarchical data structure that concatenates features from each layer to achieve a scene representation at different levels of detail. A similar approach is NSVF [43], which constructs sparse voxel meshes with geometric features. Point-NeRF [44] combines point-cloud and NeRF for fast convergence and rendering with generalization. For any 3D location, the neural points in its neighborhood are aggregated using MLP to regress the volume density and view-dependent radiation. Plenoxels [45] exploits spherical harmonics to parameterize the directional coding, bypassing the use of MLP to improve speed. Instant-NGP [17] demonstrates that neural radiation fields can be trained in real-time using a hash-based hierarchical volumetric representation of the scene. Several studies [46]–[50] have also proposed replacing the density field with a signed distance function or other representation to improve 3D reconstruction.

Similar to Co-SLAM [14], our approach employs one-blob to encode spatial coordinates on top of a multi-resolution hash grid [17] representation of the scene to achieve superior model representativeness and ensemble consistency.

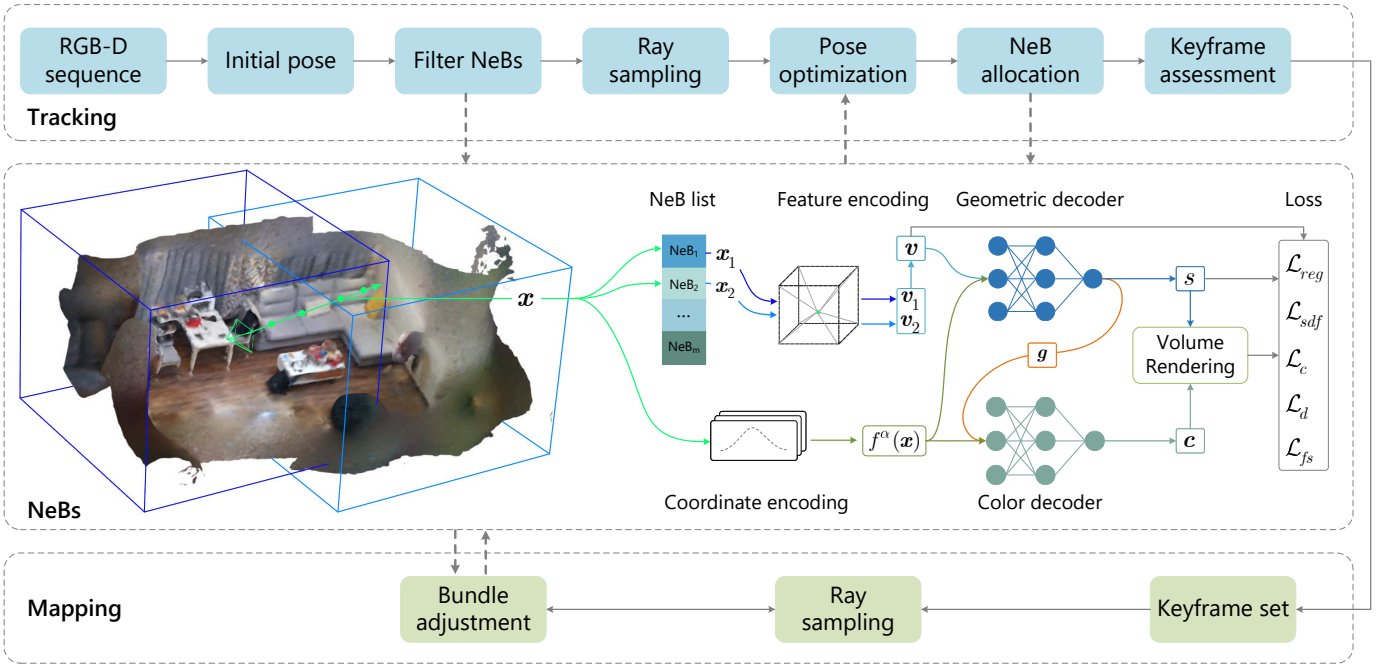


Fig. 2: Overview of NeB-SLAM. The scene is represented using NeBs, each of which has independent local coordinates and feature encoding. For any 3D point, feature encoding and coordinate encoding are used to estimate the sdf value and color by two compact MLPs. Tracking process optimizes the camera pose for each frame, and mapping process jointly optimizes the scene representation and the poses of all keyframes.

C. Neural Implicit SLAM

Decoupling the dependence on known camera poses has become another research topic in the area of neural radiation fields. This is particularly tempting for NeRF because the acquisition of the poses of the images usually requires additional preprocessing, which is usually done with COLMAP [51].

iNeRF [52] was the first system to show that it is possible to regress the camera pose in the case of a trained NeRF for a given scene. In actuality, it is not considered a full slam system, but rather a localization problem under an existing model. Barf [53] further showed how to fit the NeRF while estimating the camera pose given an inaccurate initial guess by establishing a theoretical connection from classical image alignment to joint alignment and reconstruction with neural radiance field. To be precise, the method solves the structure from motion (SfM) problem. The aforementioned methods choose large MLPs as map representations and are therefore too slow for online inference.

iMAP [11] demonstrates the application of NeRF in reconstructing precise 3D geometry from RGB-D images without poses for the first time. iMAP directly uses a single MLP to approximate a global scene and jointly optimizes the map and the camera poses. However, the use of a single MLP makes it difficult to represent geometric details of the scene as well as scale to larger environments without significantly increasing the network capacity. NICE-SLAM [12] proposes to tackle the scalability problem by subdividing the world coordinate frame into uniform grids in order to make inference faster and more accurate. NeRF-SLAM [13] combines Droid-SLAM [36] with Instant-NGP [17], using Droid-SLAM to estimate camera

poses, dense depth maps and their uncertainties, and using the above information to optimize the Instant-NGP scene representations. The GO-SLAM [54] improves global consistency in scene reconstruction by introducing loop closure and global bundle adjustment. Co-SLAM [14] combines the advantages of coordinates and sparse grid encoding to achieve high quality reconstruction of the scene.

All of the previous methods require the bounding box of the scene in order to normalize a feature space. In contrast, our approach is specifically designed for unknown scenes. This means that it can still work even if the spatial dimension information of the scene is not known.

III. METHOD

Given a set of RGB-D image sequences $\{I_t, D_t\}_{t=1}^N$ (I and D are the color and depth images, respectively) as input, our goal is to output a surface reconstruction of the scene, as well as a trajectory of the 6 DoF camera poses $T_t = [R_t | t_t]$ ($[R | t] \in SE(3)$). Fig. 2 presents an overview of our approach. The map is composed of NeBs, each of which is a fixed-size cube defined in a local coordinate frame with spatial features encoded by a multi-resolution hash grid [17]. These NeBs are adaptively allocated and progressively cover the entire unknown scene as the camera tracking.

Similar to other SLAM systems, our approach consists of two distinct processes: a tracking process that estimates the current camera pose and a mapping process that optimizes the global map. At system startup, the global map is initialized through a few mapping iterations for the first frame. For subsequent frames, the tracking process uses the NeBs

corresponding to the current frame and the differential volume rendering method to estimate its pose. It determines for each frame whether it is a keyframe or not and decides if a new NeB should be allocated or not. The mapping process receives new key frames and optimizes the map (NeBs) globally.

A. Neural Blocks

We represent the unknown scene with a set of NeBs $\{B_m\}_{m=1}^M$ that are adaptively allocated along the camera trajectory. Each NeB $B_m = (\mathbf{C}_m, \mathcal{F}_m, f^\alpha, f_m^\beta, f^\gamma, f^\delta)$ is a multi-resolution hash grid defined in its respective local coordinate frame. Here, $\mathbf{C}_m \in \mathbb{R}^3$ refers to the center coordinate of each neural block as defined in the world coordinate frame, and \mathcal{F}_m denotes the sequence of keyframes corresponding to each NeB, with each keyframe including its pose \mathbf{T}_t in the world coordinate frame, as well as a color image and a depth image. f_m^β represents the multi-resolution hash encoding [17] for the corresponding NeB that encodes any local coordinate as a feature vector. Given a 3D point $\mathbf{x} \in \mathbb{R}^3$ in the world frame, the encoding feature vector in m^{th} NeB is $\mathbf{v}_m = \{\mathbf{v}_{ml}\}_{l=1}^L = f_m^\beta(\mathbf{x}_m)$, where \mathbf{x}_m refers to the local coordinate of \mathbf{x} in the coordinate frame of B_m . The encoding feature vector \mathbf{v}_{ml} in the level l with resolution R_l is defined as:

$$\begin{aligned} \mathbf{v}_{ml} &= \sum_{i=1}^8 w(\mathbf{x}_{ml}^i) h(\mathbf{x}_{ml}^i), \\ [\mathbf{x}_{ml}] &:= \lfloor \mathbf{x}_m R_l \rfloor, [\mathbf{x}_{ml}] := \lceil \mathbf{x}_m R_l \rceil, \\ R_l &:= \lfloor R_{min} b^l \rfloor, b := \exp\left(\frac{\ln R_{max} - \ln R_{min}}{L-1}\right), \end{aligned} \quad (1)$$

where R_{min} and R_{max} are the minimum and maximum resolution of the hash grid, L is the number of levels. \mathbf{x}_{ml}^i denotes the neighboring grid point around \mathbf{x}_{ml} for trilinear interpolation, and $w(\mathbf{x}_{ml}^i)$ is the corresponding weight. h represents the hash function [17], [55] to retrieve the feature vector at \mathbf{x}_{ml}^i . Similar to [14], Spatial coordinates in world frame are encoded using One-blob encoding f^α for coherence and smoothness reconstruction. With the encoded features above, the geometric decoder f^γ predicts the SDF value s_m and the feature vector \mathbf{g}_m at \mathbf{x} :

$$f^\gamma(f^\alpha(\mathbf{x}), f_m^\beta(\mathbf{x}_m)) \mapsto (s_m, \mathbf{g}_m). \quad (2)$$

Then, the color MLP f^δ predicts the RGB value \mathbf{c}_m :

$$f^\delta(f^\alpha(\mathbf{x}), \mathbf{g}_m) \mapsto \mathbf{c}_m. \quad (3)$$

Here, the parameters in f_m^β , f^γ and f^δ are learnable.

B. Rendering for Neural Blocks

Similar to other methods [11], [12], [14], the depth and color maps are obtained through differentiable volume rendering, which integrates the SDFs and colors obtained in Sec. III-A. Specifically, Given the camera intrinsic parameters \mathbf{K} and camera pose $\mathbf{T} = [\mathbf{R}|\mathbf{t}]$, the ray origin \mathbf{o} and direction \mathbf{r} corresponding to each pixel coordinate $[u, v]$ can be obtained:

$$\begin{aligned} \mathbf{o} &= \mathbf{t}, \\ \mathbf{r} &= \mathbf{R}\mathbf{K}^{-1}[u, v, 1]^\top. \end{aligned} \quad (4)$$

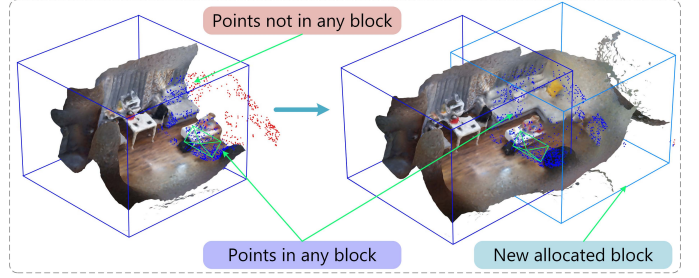


Fig. 3: NeB allocation. NeBs are adaptively allocated based on the proportion of newly observed scene to the whole scene in the current viewing frustum.

Along this ray, we sample N_1 points uniformly between the *near* and *far* bound of the viewing frustum. Additionally, we further sample N_2 points near the surface uniformly for rays with valid depth values. Thus, a total of $N_p = N_1 + N_2$ points are sampled on each ray. These sampling points can be written as $\mathbf{x}_i = \mathbf{o} + d_i \mathbf{r}, i \in \{1, \dots, N_p\}$, and d_i corresponds to the depth value of \mathbf{x}_i along this ray. For each point \mathbf{x}_i on the ray, the SDF and color values can be calculated using Eq. (2) and Eq. (3), and the corresponding depth and color values of the ray can be obtained by volume rendering:

$$\begin{aligned} \hat{d} &= \frac{1}{\sum_{i=1}^{N_p} w_i} \sum_{i=1}^{N_p} w_i d_i, \\ \hat{\mathbf{c}} &= \frac{1}{\sum_{i=1}^{N_p} w_i} \sum_{i=1}^{N_p} w_i \mathbf{c}_i, \\ w_i &= \sigma\left(\frac{s_i}{tr}\right) \sigma\left(-\frac{s_i}{tr}\right), \end{aligned} \quad (5)$$

where $\{w_i\}_{i=1}^{N_p}$ are the weights of the corresponding depths $\{d_i\}_{i=1}^{N_p}$ along the ray and tr is the truncation distance. Following [50], we multiply the two Sigmoid functions $\sigma(\cdot)$ to compute the weights w_i .

As previously stated, a set of adaptively allocated NeBs is employed to represent the unknown scene. As illustrated in and Fig. 2, with respect to a given point \mathbf{x} on a ray, there may be more than one NeB $\{B_m\}_{m=1}^M$ to which it is assigned, or there may be only one. In the former case, the feature vectors are extracted from the NeBs in separate instances and the mean value is taken as the output of the point $\mathbf{v}_x = \frac{1}{M} \sum_{m=1}^M f_m^\beta(\mathbf{x}_m)$, where $\mathbf{x}_m = \mathbf{x} - \mathbf{C}_m$ is the local coordinate in the corresponding NeB. For the latter, the feature vector of the point is computed in the corresponding NeB $\mathbf{v}_x = f_m^\beta(\mathbf{x}_m)$. Subsequently, Eq. (2) and Eq. (3) are employed to obtain the corresponding SDFs and colors, and Eq. (5) is used to derive the depths and colors of the volume rendering. In the aforementioned procedure, we limit our consideration to candidate NeBs within the viewing frustum. Additionally, points that are within the viewing frustum but not included in either NeB are discarded during the sampling process.

C. Neural Block Allocation

The NeB is an axis-aligned cube of fixed size ($5 \times 5 \times 5$ m³ in our experiments) and we adaptively allocate NeBs along the

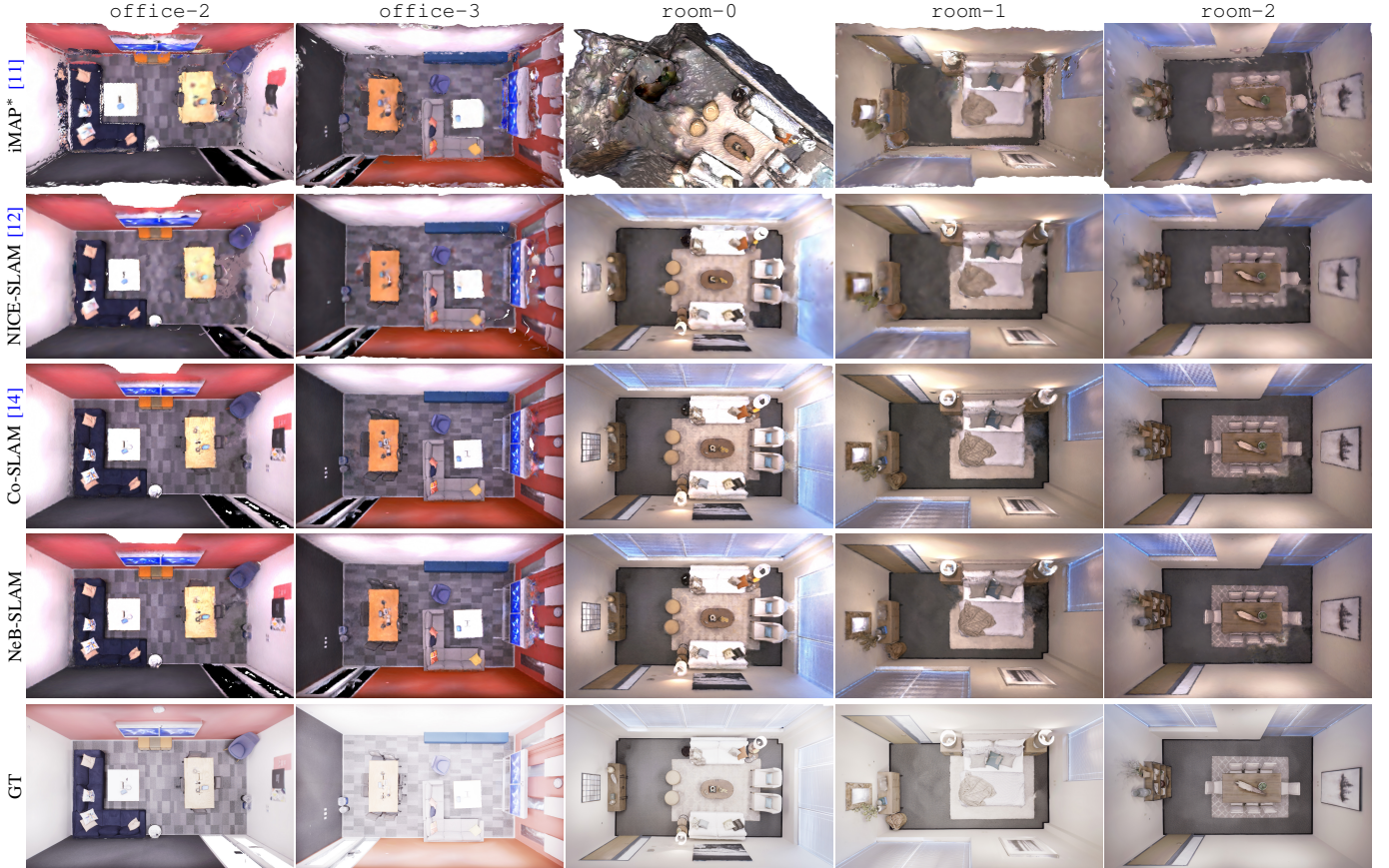


Fig. 4: Partial reconstruction results on Replica dataset [56]. All baseline methods are based on known scene size. Our method, however, is capable of obtaining complete, accurate, and high-quality reconstruction results without the need for scene size.

camera trajectory for unknown scenes during camera tracking. For each frame with a pose \mathbf{T} and intrinsic parameters \mathbf{K} , we determine whether to allocate a new NeB by a metric τ that is the ratio of the newly observed scene to the whole scene in current viewing frustum as shown in Fig. 3. Specifically, we first select a random pixels with valid depths $\{D[u_i, v_i]\}$ ($[u_i, v_i]$ is the i^{th} pixel coordinate) in current frame and then back-project them into the world coordinate frame to obtain a 3D point set $\mathcal{X} = \{\mathbf{x}_i\}$, here $\mathbf{x}_i = D[u_i, v_i] \mathbf{T} \mathbf{K}^{-1} [u_i, v_i, 1]^{\top}$. Then, we compute the ratio τ as:

$$\tau = \frac{|\mathcal{X}| - \sum_{i=1}^{|\mathcal{X}|} \mathbb{I}(\mathbf{x}_i \in \mathcal{B})}{|\mathcal{X}|}, \quad (6)$$

where \mathcal{B} denotes the set of all the 3D points in NeBs within the current viewing frustum. \mathbb{I} is an indicator function that results in 1 if \mathbf{x}_i belongs to the set \mathcal{B} and 0 otherwise. If τ is greater than a threshold τ_{th} , a new NeB is allocated with center \mathbf{C} :

$$\mathbf{C} = \frac{1}{|\mathcal{X} \setminus \mathcal{B}|} \sum_{\mathbf{x} \in \mathcal{X} \setminus \mathcal{B}} \mathbf{x}. \quad (7)$$

D. Tracking and Mapping

During the tracking and mapping, we optimize the camera poses $\{\mathbf{T}_t\}$ and the scene geometry parameters $\{f_m^\beta\}$, as well as the network parameters f^γ and f^δ , by minimizing the objective function. For the sampled set of pixels $\mathcal{P} = \{[u_i, v_i]\}$

with corresponding colors $\{c_i\}$ and depths $\{d_i\}$, a ray is generated for each pixel using the corresponding camera pose via Eq. (4) and N_p points are sampled on each ray. The depth loss \mathcal{L}_d and color loss \mathcal{L}_c are defined as the L_2 losses between the observation and the results rendered by Eq. (5):

$$\begin{aligned} \mathcal{L}_c &= \frac{1}{|\mathcal{P}|} \sum_{i=1}^{|\mathcal{P}|} (c_i - \hat{c})^2, \\ \mathcal{L}_d &= \frac{1}{|\mathcal{R}|} \sum_{r \in \mathcal{R}} (d_r - \hat{d}_r)^2, \end{aligned} \quad (8)$$

where \mathcal{R} denotes the set of pixels with valid depth measurements in \mathcal{P} . For points within the truncation region $\mathcal{X}^{tr} = \{\mathbf{x} \mid |d_i - d_x| \leq tr\}$, we calculate the SDF loss:

$$\mathcal{L}_{sdf} = \frac{1}{|\mathcal{R}|} \sum_{r \in \mathcal{R}} \frac{1}{|\mathcal{X}_r^{tr}|} \sum_{\mathbf{x} \in \mathcal{X}_r^{tr}} (s_x - \hat{s}_x)^2, \quad (9)$$

where \hat{s}_x is the predicted SDF value of the point \mathbf{x} and $s_x = d_i - d_x$ is the observed SDF value. For points not in the truncation region $\mathcal{X}^{fs} = \{\mathbf{x} \mid |d_i - d_x| > tr\}$, similar to [14], [50], a free-space loss is applied, which forces the SDF prediction to be the truncated distance tr :

$$\mathcal{L}_{fs} = \frac{1}{|\mathcal{R}|} \sum_{r \in \mathcal{R}} \frac{1}{|\mathcal{X}_r^{fs}|} \sum_{\mathbf{x} \in \mathcal{X}_r^{fs}} (s_x - tr)^2, \quad (10)$$

Furthermore, to prevent the occurrence of noisy reconstruction due to hash collisions in unobserved free-space regions,

TABLE I: Reconstruction results on Replica [56] and Synthetic RGBD [50] datasets. **NeB-SLAM** and **NeB-SLAM[†]** denote our methods with hash sizes of 15 and 14, respectively. Best results are highlighted as **first**, **second**, and **third**. Our method exhibits more favorable results.

Methods	Metrics	Replica									Synthetic							
		r0	r1	r2	o0	o1	o2	o3	o4	Avg.	BR	CK	GR	GWR	MA	TG	WR	Avg.
iMap*	Depth L1[cm]↓	6.85	5.83	6.31	6.37	4.22	6.20	8.57	6.64	6.37	23.80	63.11	30.32	35.93	56.61	19.88	65.83	42.21
	Acc.[cm]↓	5.72	4.02	5.39	4.16	6.38	5.95	5.35	5.38	5.29	10.29	30.16	13.16	21.68	15.13	13.97	37.85	20.32
	Comp.[cm]↓	5.33	5.70	5.49	4.15	5.02	6.74	5.44	6.39	5.53	13.42	37.79	16.51	26.13	43.18	15.25	31.54	26.26
	Comp. Ratio[<5cm%]↑	77.93	76.82	79.08	81.14	79.74	75.08	72.06	73.02	76.86	38.05	13.84	32.47	17.96	12.58	28.32	12.37	22.23
NICE-SLAM	Depth L1[cm]↓	2.63	1.43	2.22	1.94	4.95	2.78	2.64	2.16	2.59	5.27	15.30	3.00	2.50	2.21	9.93	6.59	6.40
	Acc.[cm]↓	2.38	2.03	2.18	1.79	1.78	3.09	2.99	2.68	2.37	2.53	11.08	2.20	2.69	1.78	5.10	7.03	4.63
	Comp.[cm]↓	3.01	2.31	2.71	2.44	2.34	3.04	3.26	3.73	2.86	5.03	14.49	4.37	3.11	3.53	7.30	5.68	6.22
	Comp. Ratio[<5cm%]↑	90.74	93.08	90.76	92.56	92.13	87.75	86.54	86.24	89.98	84.44	51.70	85.69	88.25	82.27	59.53	70.61	74.64
Co-SLAM	Depth L1[cm]↓	0.99	0.89	2.28	1.21	1.45	1.78	1.60	1.45	1.46	3.43	6.55	1.96	1.36	1.33	4.85	3.04	3.22
	Acc.[cm]↓	2.01	1.60	1.90	1.54	1.27	2.69	2.74	2.31	2.01	2.04	4.49	1.96	1.99	1.60	5.61	6.14	3.40
	Comp.[cm]↓	2.17	1.84	1.94	1.53	1.64	2.47	2.69	2.49	2.10	1.93	5.05	2.73	2.32	2.66	2.67	3.46	2.97
	Comp. Ratio[<5cm%]↑	94.35	95.2	93.72	96.36	94.48	91.87	91.15	90.95	93.51	95.21	67.45	91.90	94.15	87.03	86.82	83.61	86.60
NeB-SLAM	Depth L1[cm]↓	0.97	0.77	2.31	1.22	1.39	1.75	1.58	1.47	1.43	3.21	5.72	2.06	1.24	1.37	4.47	3.40	3.07
	Acc.[cm]↓	1.99	1.57	1.89	1.52	1.26	2.70	3.23	2.28	1.97	2.06	4.29	1.69	1.88	1.59	2.73	7.04	3.04
	Comp.[cm]↓	2.12	1.76	1.95	1.53	1.62	2.39	2.71	2.48	2.07	2.15	6.01	3.07	2.26	2.68	2.48	3.15	3.11
	Comp. Ratio[<5cm%]↑	94.59	95.46	93.56	96.32	94.62	92.10	91.06	91.18	93.61	94.52	66.63	89.80	94.56	86.92	87.90	84.06	86.34
NeB-SLAM [†]	Depth L1[cm]↓	1.02	0.72	2.33	1.18	1.43	2.09	1.56	1.44	1.47	3.38	6.13	1.99	1.31	1.38	4.50	3.48	3.17
	Acc.[cm]↓	2.06	1.60	1.93	1.53	1.30	2.74	2.87	2.27	2.04	2.10	4.35	1.87	2.02	1.55	2.79	5.47	2.88
	Comp.[cm]↓	2.06	1.75	1.94	1.55	1.58	2.42	2.72	2.52	2.06	2.25	5.21	3.53	2.30	2.62	2.57	3.78	3.18
	Comp. Ratio[<5cm%]↑	94.79	95.39	93.52	96.27	94.84	91.12	91.6	90.98	93.56	94.57	67.19	89.89	94.23	87.29	87.27	83.66	86.30

following [14], we randomly select a set of points \mathcal{X}^g and perform regularization on the corresponding interpolated features $v_{\mathbf{x}} = \frac{1}{M} \sum_{m=1}^M f_m^\beta(\mathbf{x} - \mathbf{C}_m)$:

$$\mathcal{L}_{reg} = \frac{1}{|\mathcal{X}^g|} \sum_{\mathbf{x} \in \mathcal{X}^g} (\Delta_x^2 + \Delta_y^2 + \Delta_z^2), \quad (11)$$

where $\Delta_{x,y,z} = v_{\mathbf{x}+\epsilon_{x,y,z}} - v_{\mathbf{x}}$ denotes the feature-metric difference between adjacent sampled vertices on the hash-grid along the three dimensions. In summary, the objective of our optimization process is to minimize a combination of the aforementioned losses:

$$\mathcal{L} = \lambda_1 \mathcal{L}_c + \lambda_2 \mathcal{L}_d + \lambda_3 \mathcal{L}_{sdf} + \lambda_4 \mathcal{L}_{fs} + \lambda_5 \mathcal{L}_{reg}, \quad (12)$$

here $\lambda_{1,2,3,4,5}$ are the corresponding weights.

Tracking. During tracking, we estimate the camera pose T_t for each frame. When a new frame comes in, the pose of the current frame t is initialized using the constant velocity assumption:

$$T_t = T_{t-1} T_{t-2}^{-1} T_{t-1}, \quad (13)$$

Then, a random selection of pixels N_t is made, and sample points are generated. The corresponding estimates are rendered by the method described in Sec. III-B. Finally, the camera pose is optimized iteratively by minimizing the objective function Eq. (12). For each frame, following the optimization of its pose, a determination is made as to whether a new NeB should be allocated by the method described in Sec. III-C. In the pose optimization process, only regions covered by NeBs are sampled, and thus regions that are currently not covered by NeBs will not affect the optimization.

In the context of keyframe selection, a fixed number of frames is employed in a manner analogous to other methods. However, when a new NeB is allocated at current frame, this

frame is designated as a keyframe without the need for further selection.

Mapping. During the mapping process, we employ the keyframe data management strategy in [14]. Instead of storing the complete keyframe image, only a subset of pixels is stored to represent each keyframe. This approach enables more frequent insertion of new keyframes and maintains a larger keyframe database. For joint optimization, we randomly sample N_m rays from the global keyframe list to optimize our scene representation $\{f_m^\beta\}$, MLPs f^γ , f^δ and camera poses $\{T_t\}$. The rendering approach and the optimization objective function are identical to those employed in the tracking process. Furthermore, in the event that the number of NeBs exceeds one, an additional N_a rays are collected in the keyframe sequences corresponding to the most recent NeB to be included in the joint optimization process. This is done in order to accelerate the convergence of the most recent NeB.

IV. EXPERIMENTS

A. Experimental Setup

1) *Datasets:* NeB-SLAM is evaluated on four different datasets, each containing a distinct set of scenes. Following iMAP [11], NICE-SLAM [12], and Co-SLAM [14], the reconstruction quality of 8 synthetic scenes in Replica [56] are quantified. Additionally, 7 synthetic scenes from NeuralRGBD [50] are evaluated. For the purpose of evaluating pose estimation, 6 scenes from ScanNet [57] are considered, where the ground-truth (GT) poses were obtained with BundleFusion [58], and 3 scenes from the TUM RGB-D dataset [59] are evaluated, where the GT poses were provided by a motion capture system. In addition to the aforementioned datasets, we also evaluated the reconstruction quality of our method on

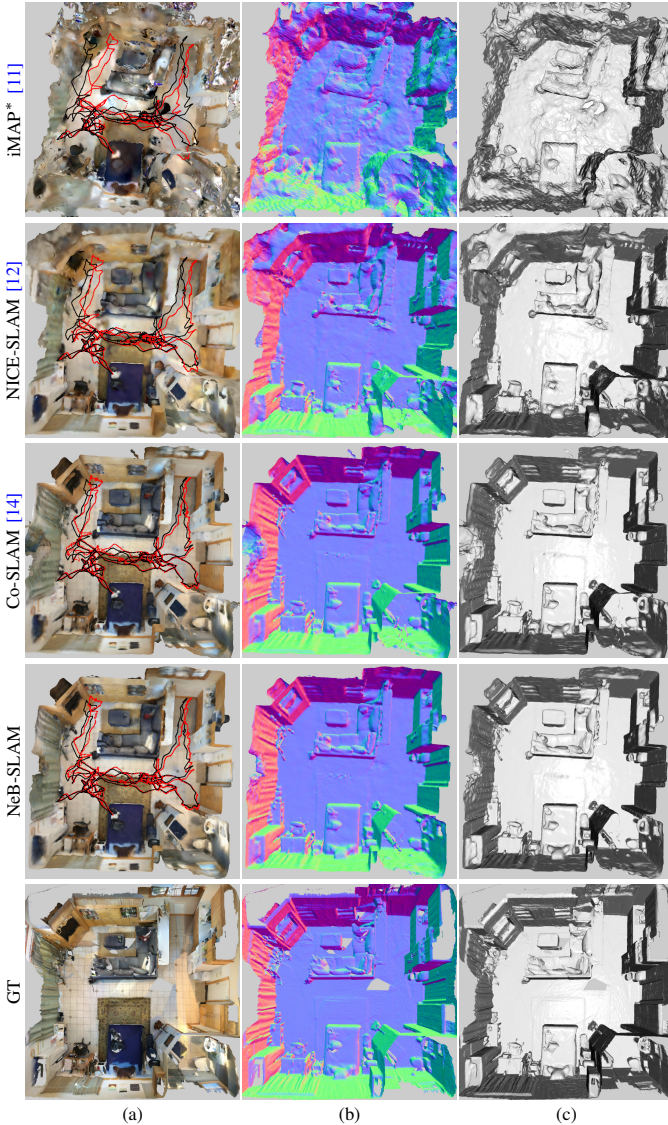


Fig. 5: Qualitative comparison on ScanNet [57] scene0000 with different shading mode. Our methods achieve accurate scene reconstruction without the need for scene size. In all the figures ground truth trajectory are shown in black and the estimated trajectory are shown in red.

the apartment dataset [12], which was collected by the Nice-SLAM authors using Azure Kinect with a larger scene size than the previous ones.

2) *Metric*: For fair comparisons, following [14], any unobserved regions outside the camera frustum and noise points within the camera frustum but outside the target scene are removed. After mesh culling, The reconstruction quality is evaluated using the following 2D and 3D metrics: **Depth L1** (cm), **Accuracy** (cm), **Completion** (cm), and **Completion Rate** (%) with a threshold of 5cm. For 2D metric, following [12], we sample $N = 1000$ virtual views from the GT and reconstructed mesh. Any views with unobserved points were rejected and resampled. The depth L1 is then defined as the average L1 difference between the rendered GT depth and the reconstructed depth. For 3D metrics, We proceed in accordance with the methodology outlined in [11], initially

TABLE II: ATE RMSE (cm) results on Replica dataset [56]. NeB-SLAM achieves better performance compared to baseline methods.

Methods	r0	r1	r2	o0	o1	o2	o3	o4	Avg.
iMap*	13.72	3.76	4.73	5.30	3.25	12.88	6.06	11.53	7.65
NICE-SLAM	2.11	4.91	1.47	1.22	1.83	2.07	4.77	1.52	2.49
Co-SLAM	0.63	1.20	0.99	0.56	0.55	2.08	1.61	0.69	1.04
NeB-SLAM	0.43	0.47	0.47	0.58	0.50	2.06	1.54	0.67	0.84
NeB-SLAM[†]	0.65	0.90	1.12	0.59	0.57	2.01	1.63	0.69	1.02

TABLE III: ATE RMSE (cm) results on Synthetic RGBD dataset [50]. Our method achieves the best tracking performance in every scene.

Methods	br	ck	gr	gwr	ma	tg	wr	Avg.
iMap*	9.21	30.57	21.23	15.73	218.60	117.14	268.45	97.28
NICE-SLAM	3.60	6.50	2.75	3.07	1.83	52.07	3.70	10.50
Co-SLAM	1.95	1.88	1.24	1.29	0.74	2.29	1.84	1.25
NeB-SLAM	1.13	1.40	0.89	0.75	0.37	0.43	1.24	0.89
NeB-SLAM[†]	1.75	1.90	1.26	1.12	1.05	1.07	1.71	1.41

sampling 200,000 points \mathcal{G} and \mathcal{R} from the GT and reconstruction meshes in a uniform manner. **Acc** is quantified as the average distance between sampled points on the reconstructed mesh and the nearest point on the GT mesh. **Comp** is evaluated as the average distance between sampled points from the GT mesh and the nearest point on the reconstructed mesh. Finally, **Comp Rate** is determined as the percentage of points in the reconstructed mesh with a completion of less than 5 cm.

$$\begin{aligned}
 \mathbf{Acc} &= \sum_{g \in \mathcal{G}} (\min_{r \in \mathcal{R}} \|g - r\|) / |\mathcal{G}| \\
 \mathbf{Comp} &= \sum_{r \in \mathcal{R}} (\min_{g \in \mathcal{G}} \|g - r\|) / |\mathcal{R}| \\
 \mathbf{Comp Rate} &= \sum_{r \in \mathcal{R}} (\min_{g \in \mathcal{G}} \|g - r\| < 0.05) / |\mathcal{R}|
 \end{aligned} \tag{14}$$

In the context of camera tracking evaluation, the absolute trajectory error (ATE) RMSE (cm) [59] is employed. Unless otherwise stated, the results are reported as the average of five runs by default.

3) *Baselines*: The present study compares the reconstruction quality and camera tracking of three different methods: iMAP [11], NICE-SLAM [12], and Co-SLAM [14]. iMAP* is the reimplement released by the authors of NICE-SLAM. Prior to the comparison, all methods implement the mesh culling strategy previously described. It is important to note that these methods are designed for known scenes, whereas our method is intended for unknown scenes. This distinction is evident in the input parameters of our method, which do not include the scene size, in contrast to the aforementioned methods.

4) *Implementation Details*: These methods are executed on a desktop PC with an Intel Core i9-14900KF CPU and NVIDIA RTX 4090 GPU. In our method (NeB-SLAM), during camera tracking, a sample of $N_t = 1024$ pixels is taken and 10 iterations are performed to optimize the camera pose. During mapping, we sample $N_m = 2048$ and $N_a = 512$ pixels, and utilize 200 iterations for the first frame mapping

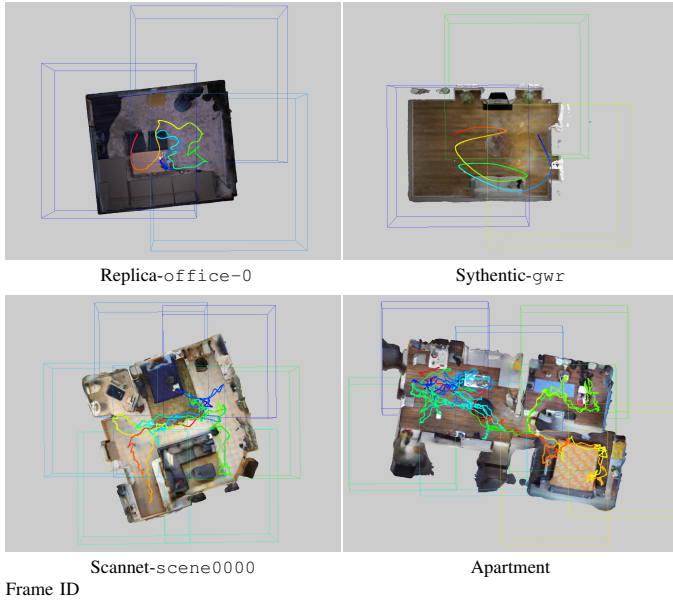


Fig. 6: NeBs allocation of our method in different scenarios.

and 10 iterations for each subsequent five frames of BA. For each ray, we uniformly sample 32 points and depth-guided sample 11 points. For each NeB ($5 \times 5 \times 5 \text{ m}^3$), a 16-level HashGrid from $R_{\min} = 16$ to R_{\max} is employed, with a maximum hash entries $T = 2^{15}$ per level, R_{\max} is determined by the voxel size of 2 cm, and OneBlob encodes 16 bins per dimension. Additionally, we provide smaller memory versions (NeB-SLAM[†]) that utilize an $T = 2^{14}$ HashGrid for each NeB. Two 2-layer shallow MLPs with 32 neurons are utilized to decode SDFs and colors. The geometric feature \mathbf{g} has a size of 15. We optimize the camera pose using a learning rate of $1e-3$ in tracking and the feature grids, decoders, and camera poses during mapping using learning rates of $1e-2$, $1e-2$ and $1e-3$. The weights for each loss are $\lambda_c = 5$, $\lambda_d = 0.1$, $\lambda_{sdf} = 1000$, $\lambda_{fs} = 10$, and $\lambda_{reg} = 1e-6$. The truncation distance, tr , is set to 10 cm. The learning rate of camera pose in tracking for TUM dataset is set to $1e-2$ and we set tr and iterations of BA to 5 cm and 20 respectively. For ScanNet, we uniformly sample 96 points and depth-guided sample 21 points.

B. Evaluation of Tracking and Mapping

1) *Replica dataset*: Tab I presents a comparative analysis of the reconstruction accuracy of the proposed method (NeB-SLAM) with that of the baseline method on Replica dataset [56]. Our method achieves comparable outcomes to those observed in Co-SLAM, with the exception of a few scenarios where our approach demonstrates superior performance. Furthermore, our method exhibits more favorable average values for each metric within the dataset. It is observed that the less memory version (NeB-SLAM[†]) yields better results in certain instances. It is noteworthy that our approach does not require the size of the scene to be inputted, and instead relies on the proposed adaptive map growth strategy to gradually allocate NeBs to cover the entire scene. Consequently, in terms of

TABLE IV: ATE RMSE (cm) results on ScanNet dataset [57]. NeB-SLAM achieves better or on-par performance compared to baseline method

Methods	0000	0059	00106	00169	0181	0207	Avg.
iMap*	47.71	45.90	30.33	58.60	21.04	25.95	38.26
NICE-SLAM	12.29	12.25	8.02	20.23	13.41	6.01	12.04
Co-SLAM	7.54	12.17	8.85	5.79	12.89	7.03	9.05
NeB-SLAM	6.84	11.36	9.07	5.47	12.06	7.32	8.69
NeB-SLAM[†]	7.12	11.68	9.56	5.82	12.78	7.78	9.12

TABLE V: ATE RMSE (cm) results on TUM RGBD dataset [59]. Overall, our approach is better.

Methods	fr1/desk	fr2/xyz	fr3/office	Avg.
iMap*	4.07	1.97	5.20	3.75
NICE-SLAM	3.01	2.11	2.64	2.59
Co-SLAM	2.94	2.07	3.06	2.69
NeB-SLAM	3.07	1.89	2.71	2.556
NeB-SLAM[†]	3.00	1.89	2.80	2.563

memory, our method is not dominant in some scenes, as shown in Tab. VI. On this dataset, our method allocates 3.7 NeBs equally for a single scene. Since each NeB represents only a localized scene, as illustrated in Fig. 1, our method is more expressive than Co-SLAM, which employs a single hash-grid to represent the entire scene. We also evaluated the absolute trajectory error of our method on this dataset, which is also superior to other baseline methods as shown in Tab. II.

2) *Synthetic dataset*: The similar evaluations are conducted on the Synthetic [50] dataset to assess the reconstruction results and absolute accuracy errors of our method. The findings are presented in Tab. I and Tab. III. The proposed methodology demonstrates high reconstruction accuracy with the lowest ATE, despite the absence of scene dimensions as input.

3) *ScanNet and TUM datasets*: Following [12] and [14], we also evaluate the tracking accuracy of our method on ScanNet [57] and TUM [59] datasets. The results are presented in Tab. IV and Tab. V. For ScanNet dataset, 6 scenes are evaluated and compared with the baseline methods, resulting in the highest tracking accuracy in most scenes, with an average tracking frame rate of approximately 15.8 FPS. On this dataset, our method allocates an average of 5 NeBs per scene, which is less advantageous in terms of the number of parameters compared to Co-SLAM [14]. However, when targeting unknown scenes, exploring the scene using a small number of redundant parameters is unavoidable. Fig. 5 shows the qualitative comparison on ScanNet scene0000 with different shading mode. Our methods achieve accurate scene reconstruction without the need for scene size. For the TUM dataset, we evaluate 3 of the scenes with an average tracking frame rate of approximately 17.2 FPS. On average, 1.6 NeBs are allocated to each scene, and the number of parameters is less than that of Co-SLAM.

4) *Apartment dataset*: We evaluate our method on an apartment dataset collected by [12]. The dataset consists of 12595 images with a scene larger than those in the previous datasets. As illustrated in Fig. 7, Our method produces more

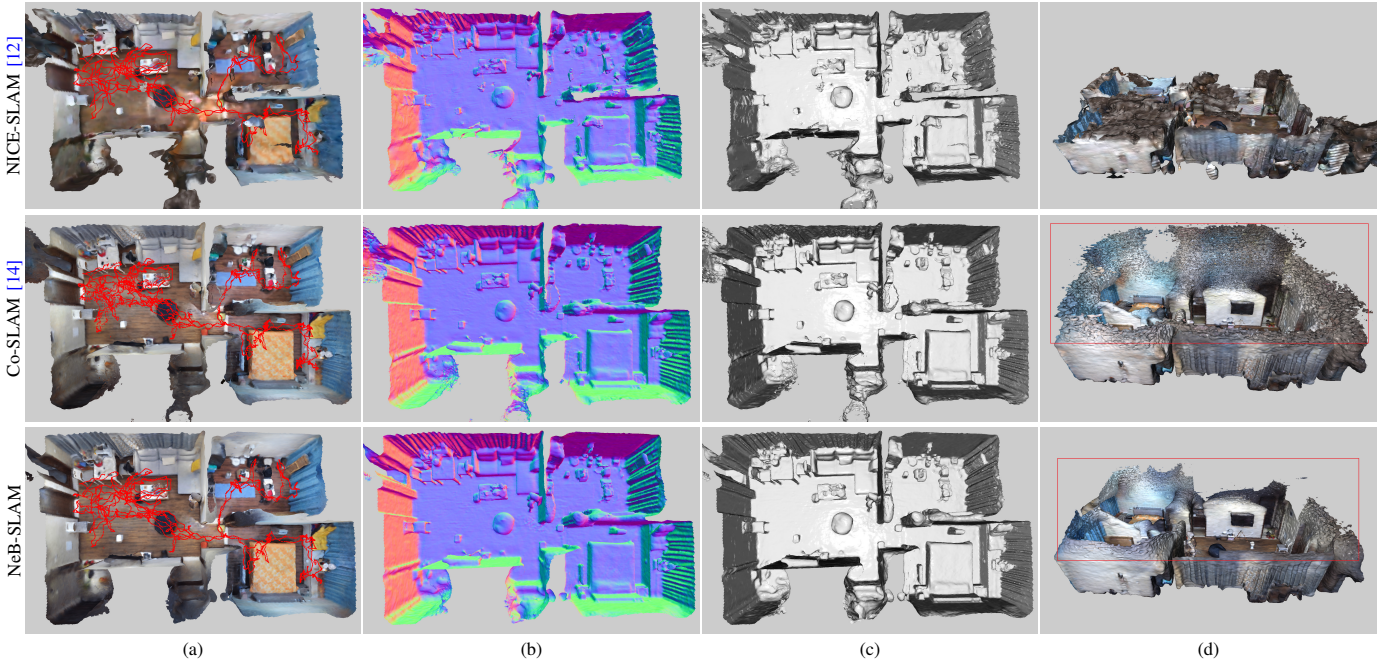


Fig. 7: Qualitative comparison on NICE-SLAM [12] apartment sequence with different shading mode. In comparison to NICE-SLAM, our method produces more refined results with enhanced quality and accuracy. In contrast to Co-SLAM, our method generates less data for unobserved regions, as illustrated in (d). It is noteworthy that our method does not require an input scene size.

TABLE VI: Run-time and memory comparison on Replica, Synthetic RGBD, ScanNet, TUM RGBD and Apartment datasets with respective settings. Run-time is reported in ms/frame / #iter. For our method, the Enc. is reported in #para / average number of NEBs.

Datasets	Methods	Track. (ms)↓	Map. (ms)↓	#param. (MB)↓	
				Enc.	Dec.
Replica	iMap*	1204.3/50	10738.8/300	/	0.85
	NICE-SLAM	58.1/10	1986.5/60	66.13	0.22
	Co-SLAM	41.8/10	74.2/10	6.33	0.02
	NeB-SLAM	48.3/10	81.4/10	12.75/3.7	0.02
	NeB-SLAM [†]	43.3/10	72.4/10	6.83/3.7	0.02
Synthetic	iMap*	1259.6/50	10698.8/300	/	0.85
	NICE-SLAM	57.2/10	1398.1/60	7.90	0.22
	Co-SLAM	42.5/10	75.5/10	6.52	0.02
	NeB-SLAM	50.8/10	92.7/10	8.74/2.5	0.02
	NeB-SLAM [†]	44.8/10	80.7/10	4.68/2.5	0.02
ScanNet	iMap*	1249/50	10477/300	/	0.85
	NICE-SLAM	391.2/50	2856.7/60	38.91	0.22
	Co-SLAM	58.3/10	138.2/10	3.01	0.02
	NeB-SLAM	63.1/10	176.1/10	17.00/5.0	0.02
	NeB-SLAM [†]	59.1/10	148.1/10	9.10/5.0	0.02
TUM	iMap*	4765.7/200	10451.2/300	/	0.85
	NICE-SLAM	5653.3/200	7279.7/60	387.41	0.22
	Co-SLAM	48.7/10	262.3/20	6.40	0.02
	NeB-SLAM	58.2/10	288.6/20	5.68/1.6	0.02
	NeB-SLAM [†]	52.2/10	271.6/20	3.04/1.6	0.02
Apartment	iMap*	1247.4/50	15516.9/300	/	0.85
	NICE-SLAM	268.7/50	2657.5/60	119.09	0.22
	Co-SLAM	45.3/10	118.1/10	41.85	0.02
	NeB-SLAM	53.8/10	132.4/10	27.2	0.02
	NeB-SLAM [†]	50.2/10	127.8/10	6.19	0.02

refined results with enhanced quality and accuracy compared to NICE-SLAM [12]. In contrast to Co-SLAM [14], our method generates less data for unobserved regions, as illustrated in Fig. 7 (d). It is noteworthy that our method does not require an input scene size. Furthermore, our method demonstrates a notable superiority with respect to the number of parameters as illustrated in Tab. VI. For scenes of greater complexity with a larger size, the number of parameters of our method increases in a manner that is nearly linear, while that of the baseline methods approach a geometric increase. Fig. 6 depicts the allocation of NeBs across various scenarios. Our method allocates NeBs sequentially along the trajectory and progressively covers the entire unknown scene.

C. Performance Analysis

On a desktop PC with an Intel Core i9-14900KF CPU and NVIDIA RTX 4090 GPU, our method (NeB-SLAM) achieves a tracking frame rate of 20 fps when utilising the default settings. For datasets that present greater challenges, such as those from Scannet and TUM, 15 FPS can still be achieved as shown in Tab. VI. In comparison to Co-SLAM, our method does not exhibit superior processing efficiency or a smaller number of parameters. However, we are able to construct a dense map of unknown environments with a minimal increase in parameters, a feat that is not achievable by all the baseline methods. Furthermore, the computational complexity of our method remains relatively constant as the number of NeBs increases, a consequence of our approach, which considers only the NeBs within the current view frustum.

D. Ablation Study

In our approach, we primarily consider the impact of hash table size T on the method. We evaluate two sizes of hash tables, as shown in Tab. VI, NeB-SLAM[†] ($T=14$) is more advantageous than NeB-SLAM ($T=15$) in terms of processing efficiency and the number of parameters in each dataset. However, NeB-SLAM yields superior results in terms of reconstruction accuracy and pose estimation. A larger hash table size was not tested since the number of parameters would be significantly higher.

V. CONCLUSION

The proposed NeB-SLAM is designed to address the challenge of constructing dense maps for unknown scenes. Our approach involves a divide-and-conquer strategy, whereby the unknown scene is divided into multiple NeBs of fixed size. These NeBs are adaptively allocated during camera tracking, gradually covering the entire unknown scene. Furthermore, when confronted with larger scenes, our method ensures the linear growth of model parameters, rather than geometric growth, while maintaining the scene representation capability of the model.

Limitations. At present, our method is only capable of adaptively assigning fixed-size NeBs. In our future work, we intend to pursue the adaptation of NeB sizes with the objective of achieving a more efficient representation of 3D scenes.

REFERENCES

- [1] S. Izadi, D. Kim, O. Hilliges, D. Molyneaux, R. Newcombe, P. Kohli, J. Shotton, S. Hodges, D. Freeman, A. Davison *et al.*, “Kinectfusion: real-time 3d reconstruction and interaction using a moving depth camera,” in *Proceedings of the 24th annual ACM symposium on User interface software and technology*, 2011, pp. 559–568.
- [2] R. A. Newcombe, S. Izadi, O. Hilliges, D. Molyneaux, D. Kim, A. J. Davison, P. Kohli, J. Shotton, S. Hodges, and A. Fitzgibbon, “Kinectfusion: Real-time dense surface mapping and tracking,” in *2011 10th IEEE international symposium on mixed and augmented reality*. Ieee, 2011, pp. 127–136.
- [3] T. Schops, T. Sattler, and M. Pollefeys, “Bad slam: Bundle adjusted direct rgb-d slam,” in *Proceedings of the IEEE/CVF Conference on Computer Vision and Pattern Recognition*, 2019, pp. 134–144.
- [4] T. Whelan, S. Leutenegger, R. F. Salas-Moreno, B. Glocker, and A. J. Davison, “Elasticfusion: Dense slam without a pose graph,” in *Robotics: science and systems*, vol. 11. Rome, Italy, 2015, p. 3.
- [5] W. Thomas, K. Michael, F. Maurice, J. Hordur, L. John, and M. John, “Kintinuous: Spatially extended kinectfusion,” in *Proceedings of RSS Workshop on RGB-D: Advanced Reasoning with Depth Cameras*, 2012.
- [6] L. Mescheder, M. Oechsle, M. Niemeyer, S. Nowozin, and A. Geiger, “Occupancy networks: Learning 3d reconstruction in function space,” in *Proceedings of the IEEE/CVF conference on computer vision and pattern recognition*, 2019, pp. 4460–4470.
- [7] S. Peng, M. Niemeyer, L. Mescheder, M. Pollefeys, and A. Geiger, “Convolutional occupancy networks,” in *Computer Vision—ECCV 2020: 16th European Conference, Glasgow, UK, August 23–28, 2020, Proceedings, Part III 16*. Springer, 2020, pp. 523–540.
- [8] J. Sun, Y. Xie, L. Chen, X. Zhou, and H. Bao, “Neuralrecon: Real-time coherent 3d reconstruction from monocular video,” in *Proceedings of the IEEE/CVF conference on computer vision and pattern recognition*, 2021, pp. 15 598–15 607.
- [9] Z. Murez, T. Van As, J. Bartolozzi, A. Sinha, V. Badrinarayanan, and A. Rabinovich, “Atlas: End-to-end 3d scene reconstruction from posed images,” in *Computer Vision—ECCV 2020: 16th European Conference, Glasgow, UK, August 23–28, 2020, Proceedings, Part VII 16*. Springer, 2020, pp. 414–431.
- [10] B. Mildenhall, P. P. Srinivasan, M. Tancik, J. T. Barron, R. Ramamoorthi, and R. Ng, “Nerf: Representing scenes as neural radiance fields for view synthesis,” *Communications of the ACM*, vol. 65, no. 1, pp. 99–106, 2021.
- [11] E. Sucar, S. Liu, J. Ortiz, and A. J. Davison, “imap: Implicit mapping and positioning in real-time,” in *Proceedings of the IEEE/CVF International Conference on Computer Vision*, 2021, pp. 6229–6238.
- [12] Z. Zhu, S. Peng, V. Larsson, W. Xu, H. Bao, Z. Cui, M. R. Oswald, and M. Pollefeys, “Nice-slam: Neural implicit scalable encoding for slam,” in *Proceedings of the IEEE/CVF Conference on Computer Vision and Pattern Recognition*, 2022, pp. 12 786–12 796.
- [13] A. Rosinol, J. J. Leonard, and L. Carlone, “Nerf-slam: Real-time dense monocular slam with neural radiance fields,” in *2023 IEEE/RSJ International Conference on Intelligent Robots and Systems (IROS)*. IEEE, 2023, pp. 3437–3444.
- [14] H. Wang, J. Wang, and L. Agapito, “Co-slam: Joint coordinate and sparse parametric encodings for neural real-time slam,” in *Proceedings of the IEEE/CVF Conference on Computer Vision and Pattern Recognition*, 2023, pp. 13 293–13 302.
- [15] Z. Zhu, S. Peng, V. Larsson, Z. Cui, M. R. Oswald, A. Geiger, and M. Pollefeys, “Nicer-slam: Neural implicit scene encoding for rgb slam,” *arXiv preprint arXiv:2302.03594*, 2023.
- [16] H. Li, X. Gu, W. Yuan, L. Yang, Z. Dong, and P. Tan, “Dense rgb slam with neural implicit maps,” *arXiv preprint arXiv:2301.08930*, 2023.
- [17] T. Müller, A. Evans, C. Schied, and A. Keller, “Instant neural graphics primitives with a multiresolution hash encoding,” *ACM transactions on graphics (TOG)*, vol. 41, no. 4, pp. 1–15, 2022.
- [18] T. Müller, B. McWilliams, F. Rousselle, M. Gross, and J. Novák, “Neural importance sampling,” *ACM Transactions on Graphics (ToG)*, vol. 38, no. 5, pp. 1–19, 2019.
- [19] G. Klein and D. Murray, “Parallel tracking and mapping on a camera phone,” in *2009 8th IEEE International Symposium on Mixed and Augmented Reality*. IEEE, 2009, pp. 83–86.
- [20] R. A. Newcombe, S. J. Lovegrove, and A. J. Davison, “Dtam: Dense tracking and mapping in real-time,” in *2011 international conference on computer vision*. IEEE, 2011, pp. 2320–2327.
- [21] B. Curless and M. Levoy, “A volumetric method for building complex models from range images,” in *Proceedings of the 23rd annual conference on Computer graphics and interactive techniques*, 1996, pp. 303–312.
- [22] M. Nießner, M. Zollhöfer, S. Izadi, and M. Stamminger, “Real-time 3d reconstruction at scale using voxel hashing,” *ACM Transactions on Graphics (ToG)*, vol. 32, no. 6, pp. 1–11, 2013.
- [23] O. Kähler, V. A. Prisacariu, C. Y. Ren, X. Sun, P. Torr, and D. Murray, “Very high frame rate volumetric integration of depth images on mobile devices,” *IEEE transactions on visualization and computer graphics*, vol. 21, no. 11, pp. 1241–1250, 2015.
- [24] J. Chen, D. Bautembach, and S. Izadi, “Scalable real-time volumetric surface reconstruction,” *ACM Trans. Graph.*, vol. 32, no. 4, pp. 113–1, 2013.
- [25] M. Zeng, F. Zhao, J. Zheng, and X. Liu, “Octree-based fusion for realtime 3d reconstruction,” *Graphical Models*, vol. 75, no. 3, pp. 126–136, 2013.
- [26] E. Vespa, N. Nikolov, M. Grimm, L. Nardi, P. H. Kelly, and S. Leutenegger, “Efficient octree-based volumetric slam supporting signed-distance and occupancy mapping,” *IEEE Robotics and Automation Letters*, vol. 3, no. 2, pp. 1144–1151, 2018.
- [27] H. Zhou, B. Ummerhofer, and T. Brox, “Deeptam: Deep tracking and mapping,” in *Proceedings of the European conference on computer vision (ECCV)*, 2018, pp. 822–838.
- [28] B. Ummerhofer, H. Zhou, J. Uhrig, N. Mayer, E. Ilg, A. Dosovitskiy, and T. Brox, “Demon: Depth and motion network for learning monocular stereo,” in *Proceedings of the IEEE conference on computer vision and pattern recognition*, 2017, pp. 5038–5047.
- [29] Z. Teed and J. Deng, “Deepv2d: Video to depth with differentiable structure from motion,” *arXiv preprint arXiv:1812.04605*, 2018.
- [30] M. Bloesch, J. Czarnowski, R. Clark, S. Leutenegger, and A. J. Davison, “Codeslam—learning a compact, optimisable representation for dense visual slam,” in *Proceedings of the IEEE conference on computer vision and pattern recognition*, 2018, pp. 2560–2568.
- [31] D. P. Kingma and M. Welling, “Auto-encoding variational bayes,” *arXiv preprint arXiv:1312.6114*, 2013.
- [32] S. Zhi, M. Bloesch, S. Leutenegger, and A. J. Davison, “Scenecode: Monocular dense semantic reconstruction using learned encoded scene representations,” in *Proceedings of the IEEE/CVF Conference on Computer Vision and Pattern Recognition*, 2019, pp. 11 776–11 785.

- [33] E. Sucar, K. Wada, and A. Davison, “Nodeslam: Neural object descriptors for multi-view shape reconstruction,” in *2020 International Conference on 3D Vision (3DV)*. IEEE, 2020, pp. 949–958.
- [34] C. Tang and P. Tan, “Ba-net: Dense bundle adjustment networks,” in *International Conference on Learning Representations*, 2018.
- [35] J. Czarnowski, T. Laidlow, R. Clark, and A. J. Davison, “Deepfactors: Real-time probabilistic dense monocular slam,” *IEEE Robotics and Automation Letters*, vol. 5, no. 2, pp. 721–728, 2020.
- [36] Z. Teed and J. Deng, “Droid-slam: Deep visual slam for monocular, stereo, and rgb-d cameras,” *Advances in neural information processing systems*, vol. 34, pp. 16 558–16 569, 2021.
- [37] —, “Raft: Recurrent all-pairs field transforms for optical flow,” in *Computer Vision—ECCV 2020: 16th European Conference, Glasgow, UK, August 23–28, 2020, Proceedings, Part II 16*. Springer, 2020, pp. 402–419.
- [38] L. Koestler, N. Yang, N. Zeller, and D. Cremers, “Tandem: Tracking and dense mapping in real-time using deep multi-view stereo,” in *Conference on Robot Learning*. PMLR, 2022, pp. 34–45.
- [39] J. Engel, V. Koltun, and D. Cremers, “Direct sparse odometry,” *IEEE transactions on pattern analysis and machine intelligence*, vol. 40, no. 3, pp. 611–625, 2017.
- [40] R. Martin-Brualla, N. Radwan, M. S. Sajjadi, J. T. Barron, A. Dosovitskiy, and D. Duckworth, “Nerf in the wild: Neural radiance fields for unconstrained photo collections,” in *Proceedings of the IEEE/CVF Conference on Computer Vision and Pattern Recognition*, 2021, pp. 7210–7219.
- [41] M. Tancik, V. Casser, X. Yan, S. Pradhan, B. Mildenhall, P. P. Srinivasan, J. T. Barron, and H. Kretschmar, “Block-nerf: Scalable large scene neural view synthesis,” in *Proceedings of the IEEE/CVF Conference on Computer Vision and Pattern Recognition*, 2022, pp. 8248–8258.
- [42] T. Takikawa, J. Litalien, K. Yin, K. Kreis, C. Loop, D. Nowrouzezahrai, A. Jacobson, M. McGuire, and S. Fidler, “Neural geometric level of detail: Real-time rendering with implicit 3d shapes,” in *Proceedings of the IEEE/CVF Conference on Computer Vision and Pattern Recognition*, 2021, pp. 11 358–11 367.
- [43] L. Liu, J. Gu, K. Zaw Lin, T.-S. Chua, and C. Theobalt, “Neural sparse voxel fields,” *Advances in Neural Information Processing Systems*, vol. 33, pp. 15 651–15 663, 2020.
- [44] Q. Xu, Z. Xu, J. Philip, S. Bi, Z. Shu, K. Sunkavalli, and U. Neumann, “Point-nerf: Point-based neural radiance fields,” in *Proceedings of the IEEE/CVF conference on computer vision and pattern recognition*, 2022, pp. 5438–5448.
- [45] S. Fridovich-Keil, A. Yu, M. Tancik, Q. Chen, B. Recht, and A. Kanazawa, “Plenoxels: Radiance fields without neural networks,” in *Proceedings of the IEEE/CVF Conference on Computer Vision and Pattern Recognition*, 2022, pp. 5501–5510.
- [46] M. Oechsle, S. Peng, and A. Geiger, “Unisurf: Unifying neural implicit surfaces and radiance fields for multi-view reconstruction,” in *Proceedings of the IEEE/CVF International Conference on Computer Vision*, 2021, pp. 5589–5599.
- [47] P. Wang, L. Liu, Y. Liu, C. Theobalt, T. Komura, and W. Wang, “Neus: Learning neural implicit surfaces by volume rendering for multi-view reconstruction,” *arXiv preprint arXiv:2106.10689*, 2021.
- [48] L. Yariv, J. Gu, Y. Kasten, and Y. Lipman, “Volume rendering of neural implicit surfaces,” *Advances in Neural Information Processing Systems*, vol. 34, pp. 4805–4815, 2021.
- [49] Z. Yu, S. Peng, M. Niemeyer, T. Sattler, and A. Geiger, “Monosdf: Exploring monocular geometric cues for neural implicit surface reconstruction,” *Advances in neural information processing systems*, vol. 35, pp. 25 018–25 032, 2022.
- [50] D. Azinović, R. Martin-Brualla, D. B. Goldman, M. Nießner, and J. Thies, “Neural rgb-d surface reconstruction,” in *Proceedings of the IEEE/CVF Conference on Computer Vision and Pattern Recognition*, 2022, pp. 6290–6301.
- [51] J. L. Schonberger and J.-M. Frahm, “Structure-from-motion revisited,” in *Proceedings of the IEEE conference on computer vision and pattern recognition*, 2016, pp. 4104–4113.
- [52] L. Yen-Chen, P. Florence, J. T. Barron, A. Rodriguez, P. Isola, and T.-Y. Lin, “Inerf: Inverting neural radiance fields for pose estimation,” in *2021 IEEE/RSJ International Conference on Intelligent Robots and Systems (IROS)*. IEEE, 2021, pp. 1323–1330.
- [53] C.-H. Lin, W.-C. Ma, A. Torralba, and S. Lucey, “Barf: Bundle-adjusting neural radiance fields,” in *Proceedings of the IEEE/CVF International Conference on Computer Vision*, 2021, pp. 5741–5751.
- [54] Y. Zhang, F. Tosi, S. Mattoccia, and M. Poggi, “Go-slam: Global optimization for consistent 3d instant reconstruction,” in *Proceedings of the IEEE/CVF International Conference on Computer Vision*, 2023, pp. 3727–3737.
- [55] M. Teschner, B. Heidelberger, M. Müller, D. Pomerantes, and M. H. Gross, “Optimized spatial hashing for collision detection of deformable objects,” in *Vmv*, vol. 3, 2003, pp. 47–54.
- [56] J. Straub, T. Whelan, L. Ma, Y. Chen, E. Wijmans, S. Green, J. J. Engel, R. Mur-Artal, C. Ren, S. Verma *et al.*, “The replica dataset: A digital replica of indoor spaces,” *arXiv preprint arXiv:1906.05797*, 2019.
- [57] A. Dai, A. X. Chang, M. Savva, M. Halber, T. Funkhouser, and M. Nießner, “ScanNet: Richly-annotated 3d reconstructions of indoor scenes,” in *Proceedings of the IEEE conference on computer vision and pattern recognition*, 2017, pp. 5828–5839.
- [58] A. Dai, M. Nießner, M. Zollhöfer, S. Izadi, and C. Theobalt, “Bundlefusion: Real-time globally consistent 3d reconstruction using on-the-fly surface reintegration,” *ACM Transactions on Graphics (ToG)*, vol. 36, no. 4, p. 1, 2017.
- [59] J. Sturm, N. Engelhard, F. Endres, W. Burgard, and D. Cremers, “A benchmark for the evaluation of rgb-d slam systems,” in *2012 IEEE/RSJ international conference on intelligent robots and systems*. IEEE, 2012, pp. 573–580.